# Mass enhancement in 3*d* and *s*-*p* perovskites from symmetry breaking

Zhi Wang, Oleksandr I. Malyi, Xingang Zhao, and Alex Zunger*
*Renewable and Sustainable Energy Institute, University of Colorado, Boulder, Colorado 80309, USA*

*In some d*-electron oxides, the measured effective mass $m^*_{\text{exptl}}$ has long been known to be significantly larger than the model effective mass $m^*_{\text{model}}$ deduced from mean-field band theory, i.e., $m^*_{\text{exptl}} = \beta m^*_{\text{model}}$, where $\beta > 1$ is the "mass-enhancement" or "mass-renormalization" factor. Previous applications of density functional theory (DFT), based on a symmetry-restricted structure with the smallest number of possible magnetic, orbital, and structural degrees of freedom, missed such mass enhancement. This fact has been taken as evidence of strong electronic correlation, often described via the symmetry-restricted dynamic mean-field approach of the many-body theory, being the exclusive enabling physics. This paper uses instead a static density functional approach that does not restrict positional or spin degrees of freedom (symmetry-broken structures). This approach analyzes the contributions of different symmetry-broken modalities to mass enhancement for a few nominally highly correlated *d*-electron perovskites as well as the nominally uncorrelated, closed-shell *s*-*p* bonding perovskites. It shows that the energy-lowering symmetry-broken spin effects (e.g., nonzero local moment in the paramagnetic phase) and structural effects (e.g., atomic displacement) as described in mean-field DFT already manifest mass enhancement for both electrons and holes in a range of *d*-electron perovskites $SrVO_3$, $SrTiO_3$, $BaTiO_3$, and $LaMnO_3$, as well as *p*-electron perovskites $CsPbI_3$ and $SrBiO_3$, including both metals ($SrVO_3$) and insulators (the rest). This is revealed only when enlarged unit cells of the same parent global symmetry, which are large enough to allow for symmetry-breaking distortions and concomitant variations in spin order, are explored for their ability to lower the total energy. Positional symmetry breaking that leads to mass enhancement includes octahedral rotation in halide perovskites such as $CsPbI_3$, Jahn-Teller-like $Q_2^+$ distortion in $LaMnO_3$, and bond disproportionation in $SrBiO_3$, while magnetic symmetry breaking resulting in mass enhancement includes the formation of a distribution of local moments in $SrVO_3$ that averages to zero in the paramagnetic phase. Not all symmetry breaking leads to significant mass enhancement, e.g., the rather small octahedral rotations in the nearly perfectly cubic $SrTiO_3$ cause negligible mass enhancement, as do the paraelectric displacements in $BaTiO_3$. In principle, by ergodicity, the two descriptions, i.e., the symmetry-restricted dynamic approach with a single time-fluctuating magnetic moment and the symmetry-broken mean-field approach with a static distribution of spatially fluctuated local moments, are not mutually exclusive but are a choice of representation and consequently, a choice of computational efficiency. In approximate implementations, the symmetry-broken mean-field approach appears to remove much of what was strong correlation in dynamically correlated symmetry-restricted solutions, leaving smaller ("weak") residual correlation with respect to the exact solution.

DOI: 10.1103/PhysRevB.103.165110

## I. INTRODUCTION

The effective mass $m^*$ defined as the reciprocal of the wave vector curvature $\partial^2 E/\hbar^2 \partial k_i \partial k_j$ of the band dispersion relation $E(k)$ (where $k_i$ and $k_j$ are wave vectors) is a central quantity in condensed matter physics, widely used to characterize the band structure, carrier transport, and wave function localization [1]. Recently, this quantity has attracted attention in the context of *d*-electron correlated oxide physics, where the measured effective mass $m^*_{\text{exptl}}$ has been noted in some cases to be significantly larger than the model effective mass $m^*_{\text{model}}$, deduced from simplified mean-field band theory $m^*_{\text{exptl}} = \beta m^*_{\text{model}}$, where $\beta$ is the "mass-enhancement" or "mass-renormalization" factor. Here, $m^*_{\text{exptl}}$ are generally deduced from experiment via model assumptions (such as band parabolicity or various averages over the mass tensor), leading to different effective mass definitions in different experiments, including the mass deduced from Fermi velocity ($v_F$) as $m^* \propto 1/v_F$, from density of states (DOS) $m^* \propto [D(E)]^{2/3}$, from specific-heat coefficient $m^* \propto \gamma$, from magnetic susceptibility $\chi \propto m^*(1-\frac{m_0^2}{3m^{*2}})$, and from the band width $W \propto \frac{1}{m^*}$. Values of $\beta > 1$ were reported in the literature for Fe-based superconductors [2,3], halide perovskites [4], titanites [5–7], ruthenates [8–10], and vanadates [11–14]. These mass enhancement factors from experiment $\beta(\text{exptl/model}) = m^*_{\text{exptl}}/m^*_{\text{model}}$ were then compared with the theoretical values $\beta(\text{Theory/model}) = m^*_{\text{Theory}}/m^*_{\text{model}}$ obtained from many-body approaches (such as dynamic mean-field theory (DMFT) [15–24]). Because $m^*_{\text{model}}$ comes from the mean-field band theory, the predicted theoretical enhancement $\beta(\text{Theory/model}) > 1$ has been interpreted to be due to strong correlation effects [15–24]. For example, in DMFT, wavefunction localizes and bandwidth narrows (thus leading to mass enhancement) due to pure electronic symmetry breaking induced by the dynamic

*alex.zunger@gmail.com

 

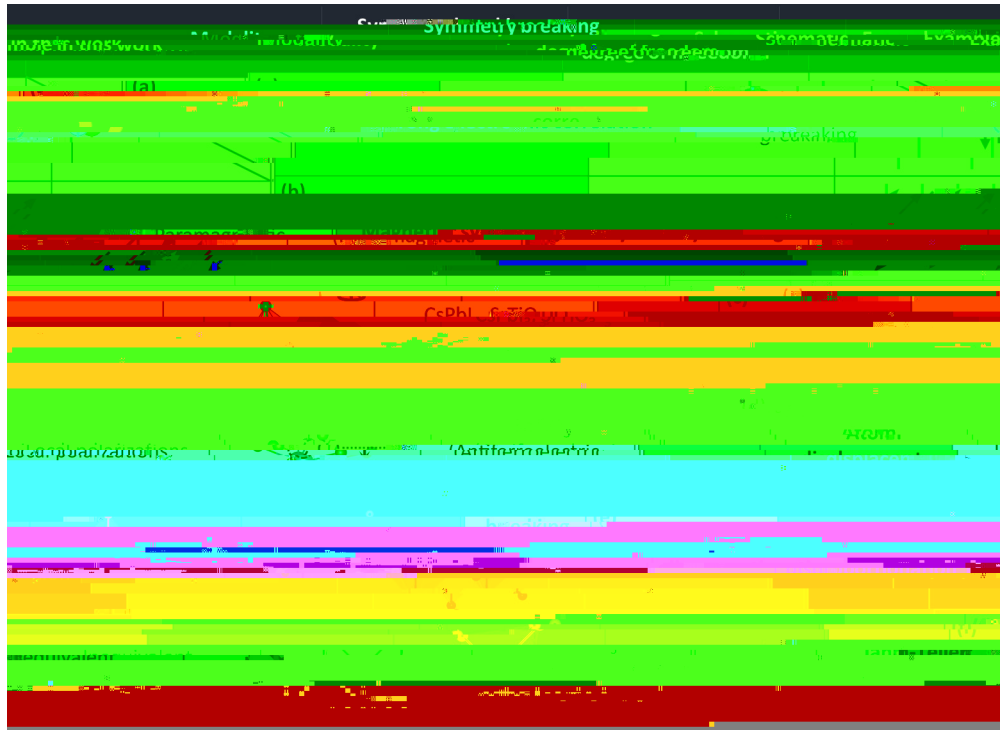

FIG. 1. Modalities of symmetry breaking illustrated for the perovskite structure. From top to bottom: (a) Strong electronic correlation as schematically shown by the Hubbard model (where $U$ is the on-site repulsion and $t$ is the hopping energy); (b) magnetic symmetry breaking such as the paramagnetism (PM), where the lattice sites are occupied by atoms having opposite spins without long-range order; (c) octahedral rotations allowing nonzero rotation angles; (d) atomic displacements such as the ferroelectric displacements in perovskites inducing a local polarization degree of freedom; (e) bond disproportionation allowing octahedra in perovskites to have different volumes; (f) Jahn-Teller distortions elongating the perovskite octahedron along one direction, leading to inequivalent bond lengths between the center and corner atoms.

leaving smaller ("weak") residual correlation with respect to the exact solution. Thus, a correlation that has been dynamic in the symmetry-restricted case can become static in the symmetry-broken cases, and the correlated methods in symmetry-restricted structures might not be the only way to describe mass enhancement [63]. Symmetry can be restored afterward [64] and often gives localized states but small ad-

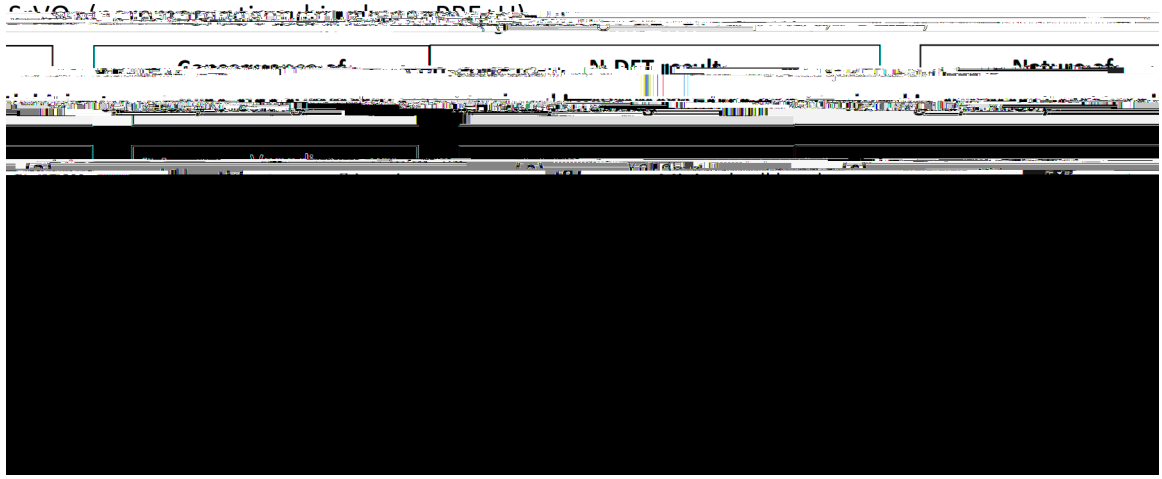

FIG. 2. Mass enhancements in the paramagnetic (PM) cubic phase of $SrVO_3$. (a) The band structure obtained from the same naïve density functional theory (N-DFT) restriction as in previous literature [12–18], namely a single-cell, cubic, nonmagnetic (NM) $SrVO_3$ model using PBE + $U$ ($U$ = 1.25 eV on V $d$ orbitals). (b) The distribution of spin moments in the present PM phase: blue lines show that, in the minimal-cell NM phase, all vanadium sites have zero magnetic moment, while the red curve shows that, in the PM phase, different vanadium sites have a distribution of different, nonzero magnetization. (c) The unfolded band structure when removing the minimal-cell restrictions by using instead a cubic, 128 f.u. PM supercell $SrVO_3$ with the same PBE + $U$ method. The total internal energy $E_{tot}$ from DFT of (c) is 31 meV per formula unit (meV/f.u.) lower than that of (a). Masses in (c) are calculated via density of states (DOS) at Fermi level (which gives $\beta_e = 1.4-1.6$ and $\beta_h = 1$; the subscripts $e$ and $h$ denote the electron and hole mass enhancements; uncertainty is due to the variation of DOS nearby the Fermi level), second derivative of $E$ vs $\mathbf{k}$ (which gives $\beta_e = 1.46$ and $\beta_h = 1$), and bandwidth (which gives $\beta_e = 1.43$ and $\beta_h = 1$). The vertical arrows in (a) and (c) show the bandwidths. The same PBE + $U$ method has been applied for all $SrVO_3$ calculations.

PM or from the DFT, and as was recently recognized, it leads

FIG. 3. Convergence of mass enhancement and band structure of $SrVO_3$ paramagnet (PM) vs supercell size increasing from 32 f.u. (160 atoms), to 64 f.u. (320 atoms), to 128 f.u. (640 atoms). All supercells are generated by using the spin special quasirandom structure (SQS) method. Note band narrowing convergence.

evolution of the unfolded band structure as the real-space supercell size increases, finding convergence.

The significant result is that the conduction band in the PM phase, allowed to have a distribution of local spin motifs, is narrowed relative to the minimal-cell NM case from 2.5 eV [Fig. 2(a)] to 1.75 eV [Fig. 2(c)]. This leads to an electron mass-enhancement factor ($\beta_e$) in the PM supercell $\beta_e$(DFT/

FIG. 4. Total density of states (DOS) of cubic $SrVO_3$ (the same PBE + $U$ method) as a weighted superposition of the partial DOS (PDOS)

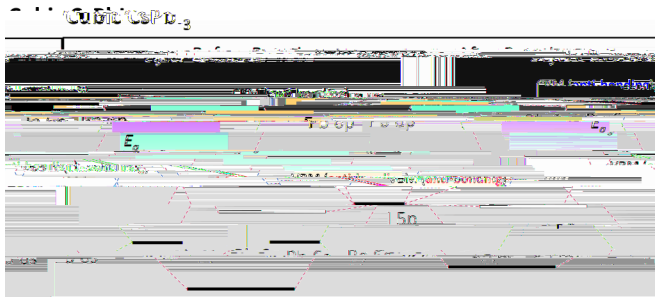

FIG. 5. Energy level diagram for $CsPbI_3$, before and after octahedral rotation. The red solid lines show the trends of band gap change.

derives from classical atomic size mismatch and therefore exists even in close-shell *s-p* electron compounds such as halide perovskites [52,90,91]. Octahedral tilting (rotation) effects have been investigated in lead and tin halide perovskites for the low-temperature tetragonal and orthorhombic phases. However, for the cubic phase, it has been generally assumed [30–33] that, because of its XRD designation as a $Pm\bar{3}m$

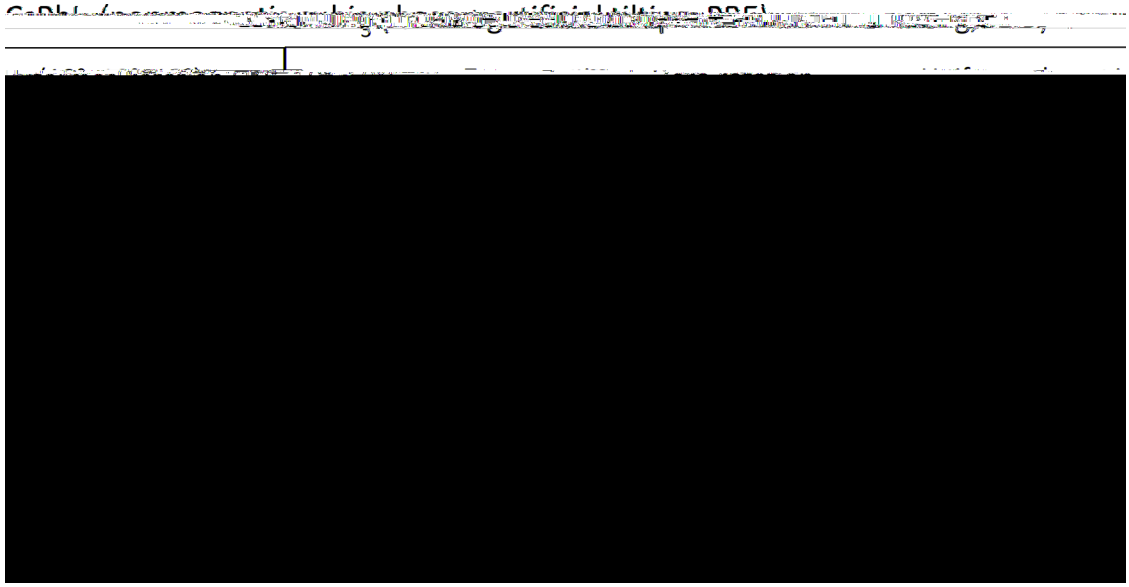

We choose $SrBiO_3$ as an example to investigate such a bond disproportionation effect on effective masses. $SrBiO_3$ is known to be insulating in its low-temperature monoclinic phase with a disproportionate $R_1^+$ distortion [106]. The monoclinic phase shows a tilting $M_3^+ \oplus R_4^+$ mode (Glazer notation $a^+b^-c^-$), which could also contribute to the mass enhancement. To isolate the contribution of $R_1^+$ disproportionation from tilting, we apply here a three-level model: (1) we start from a level 1 model, which is minimal-cell cubic $Pm\bar{3}m$ structure; (2) then we apply a tilting $M_3^+ \oplus R_4^+$ mode to construct a level 2 monoclinic ($P2_1/n$) structure without disproportionation; and (3) finally, a level 3 model uses the experimentally observed $SrBiO_3$ monoclinic phase (also $P2_1/n$) with both tilting (the same amplitude as in level 2) and disproportionation. The atomic structures, together with the band structures using the PBE functional + spin-orbit coupling (SOC) effect for these three levels, are shown in Fig. 9.

(1) Level 1 [$Pm\bar{3}m$ cubic; Figs. 9(a)

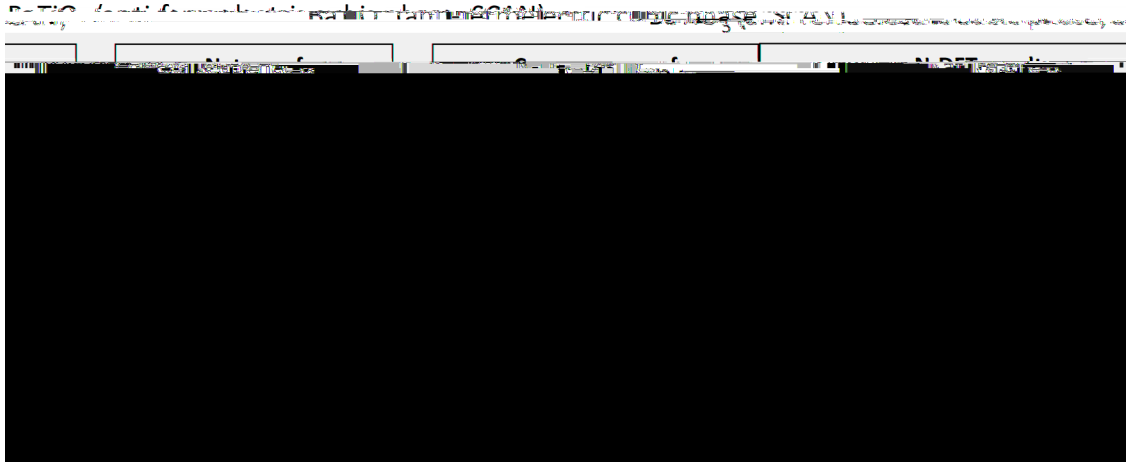

FIG. 11. Mass enhancements in antiferroelectric (AFE) cubic phase of $BaTiO_3$. (a) The band structure from the same naïve density functional theory (N-DFT) restriction as in previous literature [129–131], namely a single-cell, no Ti-atom displacement model, using SCAN functional. (b) The distribution of Ti-atom displacement symmetry breaking: upper part in (b) shows that the minimal-cell model $BaTiO_3$ does not have any Ti-atom displacement ($\Delta\mathbf{R} = 0$ for each Ti atom), while the lower part in (b) shows that the AFE supercell (8 f.u.) has a unique displacement pattern, where the eight Ti atoms move along eight ⟨111⟩ directions. In the AFE supercell, the net polarization is zero ($\langle\Delta\mathbf{R}\rangle = 0$), but the local polarization on each Ti site is large ($\langle|\Delta\mathbf{R}|\rangle = 0.13$ Å). (c) The unfolded band structure of the 8 f.u. AFE supercell $BaTiO_3$ with the same SCAN method. Masses in (c) are calculated via the second derivative of $E$ vs $\mathbf{k}$, which gives $\beta_e \approx 1.1$ and $\beta_h \approx 1$.

Γ**R**
shows a net polarization, while the eight Ti atoms move along eight 111directions.4([Tj],9.47s)2TJingl11-],9-19.874

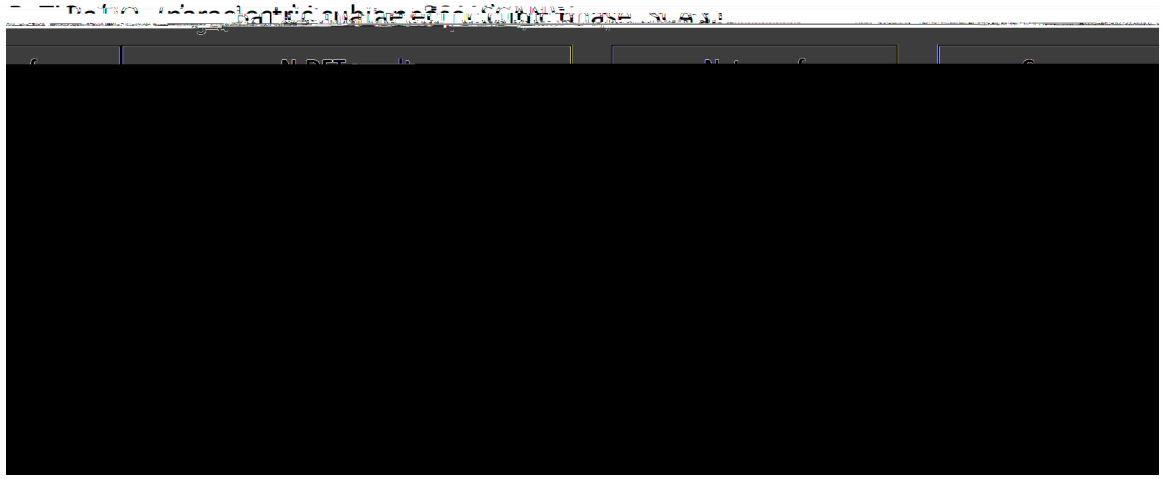

FIG. 12. Mass in the paraelectric (PE) cubic phase of $BaTiO_3$. (a) The band structure from the same naïve density functional theory (N-DFT) restriction as in previous literature [129–131], identical to Fig. 11(a). (b) The distribution of Ti-atom displacements in the 32 f.u. PE supercell after atomic relaxation along *x*, *y*, and *z* directions ([100], [010], and [001] directions). (c) The unfolded band structure of the 32 f.u. PE supercell $BaTiO_3$ with the same SCAN method. Masses in (c) are calculated via the second derivative of $E$ vs $\mathbf{k}$, which gives $\beta_e \approx 1.1$ and $\beta_h \approx 1$.

mass enhancement suggested by the high-order dynamical electron-electron correlation theory. The presence of mass enhancement in the considered systems is not necessarily evidence for the exclusive need for strong dynamically correlated methodologies [15–24].

In principle, the spin fluctuations in a nonvibrating lattice can be either (i) longitudinal (single-site spin flip or intersite spin hopping) or (ii) transversal (single-site spin rotation or spin-wave excitation). The longitudinal fluctuations can be rather fast, e.g., a few femtoseconds, in a metallic system, but slow and very rare in insulators due to the large energy cost of overcoming the band gap. The transversal fluctuations, on the other hand, are typically much slower but not significantly dependent on the metallicity, e.g., in the ordered magnetic ground state of Fe, Ni, and Co, the spin-wave excitations evolve within 1 ps [134], while in the PM state of the small-gap semiconductor CrN, individual moments rotate with respect to its neighbors in the time scale of 50–100 fs [135]. Since ARPES measurement can be done in a time scale of femtoseconds [136], spin fluctuation effects longer than this time scale (longitudinal ones in insulators and transversal ones in both insulators and metals) will be measured as the time average over many properties of individual spin configurations (average of the properties), while spin fluctuation effects shorter than a few femtoseconds (longitudinal ones in some metals) will be observed as the properties of a time-averaged spin configuration (property of the average).

For the PM phase, in a symmetry-restricted many-body approach (a) containing a single magnetic moment (monomorphous limit) interacting with an average bath, the magnetic moment must fluctuate in time to conserve the zero total moment expected of a paramagnet. In a symmetry-broken

FIG. 13. Comparison of density of states (DOS) from density functional theory (DFT) calculations using PBE + $U$ (red curve) and SCAN (blue curve) functionals for the 64 f.u. (320 atom) paramagnetic (PM) cubic supercell of $SrVO_3$. The two functionals show remarkably similar DOS at Fermi level and very similar bandwidths (denoted by the red and blue arrows).

PBE functional. Note that no SOC has been considered for $CsPbI_3$ in this paper because the PBE functional will give too small a gap (∼0.1 eV) if applied together with SOC; a better agreement with experimentally observed gap can be achieved by using SOC with a hybrid functional such as Heyd-Scuseria-Ernzerhof, which is however beyond the scope of this paper. (iv) The *s*-*p*-bonded oxide $SrBiO_3$ has been calculated using the PBE with SOC effect.

For each compound, we have applied the DFT lattice constants obtained from the minimal cell model to all supercell calculations: $a = 3.83$ Å (cubic $SrVO_3$); $a = 6.27$ Å (cubic $CsPbI_3$); $a = 5.51$ Å, $b = 5.81$ Å, and $c = 7.64$ Å ($LaMnO_3$ with Jahn-Teller-like distortion); $a = 5.57$ Å and $c = 7.87$ Å ($LaMnO_3$ without Jahn-Teller distortion); $a = 6.01$ Å, $b = 6.20$ Å, and $c = 10.49$ Å (monoclinic $SrBiO_3$); $a = 4.52$ Å (cubic $SrBiO_3$); $a = 3.91$ Å (cubic $SrTiO_3$); and $a = 4.03$ Å (cubic $BaTiO_3$). To minimize the numerical error, for all cells of the same compound in the same phase (e.g., $SrVO_3$ single f.u. cubic primitive cell vs $SrVO_3$ 64 f.u. cubic supercell),

TABLE II. Summary of DFT total energy for different collinear magnetic structures of cubic $SrVO_3$. The same PBE + $U$ method has been applied for all $SrVO_3$ calculations. All structures have the same lattice constant and atomic positions and only differ in the

[10] P. B. Allen, H. Berger, O. Chauvet, L. Forro, T. Jarlborg, A. Junod, B. Revaz, and G. Santi, Transport properties, thermodynamic properties, and electronic structure of $SrRuO_3$, Phys. Rev. B **53**, 4393 (1996).

[11] I. H. Inoue, O. Goto, H. Makino, N. E. Hussey, and M. Ishikawa, Bandwidth control in a perovskite-type $3d^1$-correlated metal $Ca_{1-x}Sr_xVO_3$ I. Evolution of the electronic properties and effective mass, Phys. Rev. B **58**, 4372 (1998).

[12] T. Yoshida, M. Hashimoto, T. Takizawa, A. Fujimori, M. Kubota, K. Ono, and H. Eisaki, Mass renormalization in the bandwidth-controlled Mott-Hubbard systems $SrVO_3$ and $CaVO_3$ studied by angle-resolved photoemission spectroscopy, Phys. Rev. B **82**, 085119 (2010).

[13] T. Yoshida, K. Tanaka, H. Yagi, A. Ino, H. Eisaki, A. Fujimori, and Z.-X. Shen, Direct Observation of the Mass Renormalization in $SrVO_3$ by Angle Resolved Photoemission Spectroscopy, Phys. Rev. Lett. **95**, 146404 (2005).

[14] T. Yoshida, M. Kobayashi, K. Yoshimatsu, H. Kumigashira, and A. Fujimori, Correlated electronic states of $SrVO_3$ revealed by angle-resolved photoemission spectroscopy, J. Electron Spectrosc. Relat. Phenom. **208**, 11 (2016).

[15] I. A. Nekrasov, K. Held, G. Keller, D. E. Kondakov, Th. Pruschke, M. Kollar, O. K. Andersen, V. I. Anisimov, and D. Vollhardt, Momentum-resolved spectral functions of $SrVO_3$ calculated by LDA + DMFT, Phys. Rev. B **73**, 155112 (2006).

[16] J. M. Tomczak, M. Casula, T. Miyake, and S. Biermann, Asymmetry in band widening and quasiparticle lifetimes in $SrVO_3$: Competition between screened exchange and local correlations from combined GW and dynamical mean-field theory GW + DMFT, Phys. Rev. B **90**, 165138 (2014).

[17] R. Sakuma, Ph. Werner, and F. Aryasetiawan, Electronic structure of $SrVO_3$ within GW + DMFT, Phys. Rev. B **88**, 235110 (2013)

[107] K. Tsuda and M. Tanaka, Refinement of crystal structure parameters using convergent-beam electron diffraction: The low-temperature phase of $SrTiO_3$, Acta Crystallogr. A **51**, 7 (1995).

[108] Yu. A. Abramov, V. G. Tsirel'son, V. E. Zavodnik, S. A. Ivanov, and I. D. Brown, The chemical bond and atomic displacements in $SrTiO_3$ from x-ray diffraction analysis, Acta Crystallogr. B **51**, 942 (1995).

[109] K. B. Lyons and P. A. Fleury, Phonon interactions and the dynamic central peak in $SrTiO_3$ near the structural phase transition, Solid State Commun. **23**, 477 (1977).

[110] A. van Roekeghem and S. Biermann, Screened exchange dynamical mean-field theory and its relation to density functional theory: $SrVO_3$ and $SrTiO_3$, EPL Europhys. Lett. **108**, 57003 (2014).

[111] A. F. Santander-Syro, O. Copie, T. Kondo, F. Fortuna, S. Pailhès, R. Weht, X. G. Qiu, F. Bertran, A. Nicolaou, A. Taleb-Ibrahimi, P. Le Fèvre, G. Herranz, M. Bibes, N. Reyren, Y. Apertet, P. Lecoeur, A. Barthélémy, and M. J. Rozenberg, Two-dimensional electron gas with universal subbands at the surface of $SrTiO_3$, Nature **469**, 189 (2011).

[112] Y. J. Chang, A. Bostwick, Y. S. Kim, K. Horn, and E. Rotenberg, Structure and correlation effects in semiconducting $SrTiO_3$, Phys. Rev. B **81**, 235109 (2010).

[113] W. Zhong and D. Vanderbilt, Competing Structural Instabilities in Cubic Perovskites, Phys. Rev. Lett. **74**, 2587 (1995).

[114] R. F. Berger, C. J. Fennie, and J. B. Neaton, Band Gap and Edge Engineering via Ferroic Distortion and Anisotropic Strain: The Case of $SrTiO_3$, Phys. Rev. Lett. **107**, 146804 (2011).

[115] J. H. Haeni, P. Irvin, W. Chang, R. Uecker, P. Reiche, Y. L. Li, S. Choudhury, W. Tian, M. E. Hawley, and B. Craigo, Room-temperature ferroelectricity in strained $SrTiO_3$, Nature **430**, 758 (2004).

[116] T. F. Nova, A. S. Disa, M. Fechner, and A. Cavalleri, Metastable ferroelectricity in optically strained $SrTiO_3$, Science **364**, 1075 (2019).

[117] A. Janotti, J. B. Varley, M. Choi, and C. G. Van de Walle, Vacancies and small polarons in $SrTiO_3$, Phys. Rev. B **90**, 085202 (2014).

[118] X. Hao, Z. Wang, M. Schmid, U. Diebold, and C. Franchini, Coexistence of trapped and free excess electrons in $SrTiO_3$, Phys. Rev. B **91**, 085204 (2015).

[119] E. Bousquet, M. Dawber, N. Stucki, C. Lichtensteiger, P. Hermet, S. Gariglio, J.-M. Triscone, and P. Ghosez, Improper ferroelectricity in perovskite oxide artificial superlattices, Nature **452**, 732 (2008).

[120] M. Zacharias, M. Scheffler, and C. Carbogno, Fully anharmonic nonperturbative theory of vibronically renormalized electronic band structures, Phys. Rev. B **102**, 045126 (2020).

[121] Y. Aiura, I. Hase, H. Bando, T. Yasue, T. Saitoh, and D. S. Dessau, Photoemission study of the metallic state of lightly electron-doped $SrTiO_3$, Surf. Sci. **515**, 61 (2002).

[122] S. A. Chambers, Y. Du, Z. Zhu, J. Wang, M. J. Wahila, L. F. J. Piper, A. Prakash, J. Yue, B. Jalan, S. R. Spurgeon, D. M. Kepaptsoglou, Q. M. Ramasse, and P. V. Sushko, Interconversion of intrinsic defects in $SrTiO_3$ (001),